DYNAMIC SHEAR RUPTURE OF STEEL PLATES

Ken Nahshon, Michael G. Pontin, Anthony G. Evans,
John W. Hutchinson and Frank W. Zok

DYNAMIC SHEAR RUPTURE OF STEEL PLATES

KEN NAHSHON, MICHAEL G. PONTIN, ANTHONY G. EVANS,
JOHN W. HUTCHINSON AND FRANK W. ZOK

Metallic sandwich panels with prismatic cores offer the potential for superior blast resistance relative to monolithic plates of equivalent areal density. However, under sufficiently high impulse, severe plastic strains can occur at the junctions of the face sheets and the core members shortly after arrival of the pressure wave but prior to significant deformation elsewhere. The potential consequence is localized shear rupture with minimal plastic dissipation. To characterize this failure mode, a combined experimental-numerical protocol has been used to ascertain the plastic strain for dynamic shear rupture of ductile metals. The experimental component involves firing cylindrical projectiles through plates of the targeted materials and monitoring changes in projectile velocity during penetration. With appropriate combinations of plate thickness and projectile velocity, penetration occurs through propagation of an annular shear crack. In parallel, a numerical model of dynamic deformation and rupture has been employed to infer the critical strain through comparisons with projectile velocity change measurements. Experiments and analyses have been performed on both 304 stainless steel and superaustenitic AL6XN. Effects of mesh size on the resolution of the predicted strain distribution and the plastic dissipation associated with penetration are addressed.

1. Introduction

Metallic sandwich panels with prismatic cores can be designed to provide resistance to underwater blasts superior to monolithic plates at equivalent areal density. The benefits derive from a reduction in the rate at which the momentum is transmitted from the water, as well as a diminution of the pressure transferred through the core to the supports [Liang et al. 2007]. These benefits require that the plastic strains in the faces as well as at the junctions of the faces with the core members remain below that needed to cause rupture (Figure 1).

Recent assessments of steel sandwich panels subject to an underwater blast exemplify the face deformations and the tendency for rupture (Figure 2) [Liang et al. 2007]. Shortly after arrival of the pressure wave, the wet face acquires uniform velocity over most of its area (see left series of images in Figure 2). However, at the attachment points to the core members, the face remains initially stationary. A consequence of the velocity difference is the development of localized plastic strains adjacent to the junctions. Rupture would occur when the plastic strain reaches a critical value (say 0.5), causing the wet face to shear-off from the core members. This would happen about 30 ms after arrival of the pressure wave. Thereafter, this face would continue moving and slap into the bottom face.
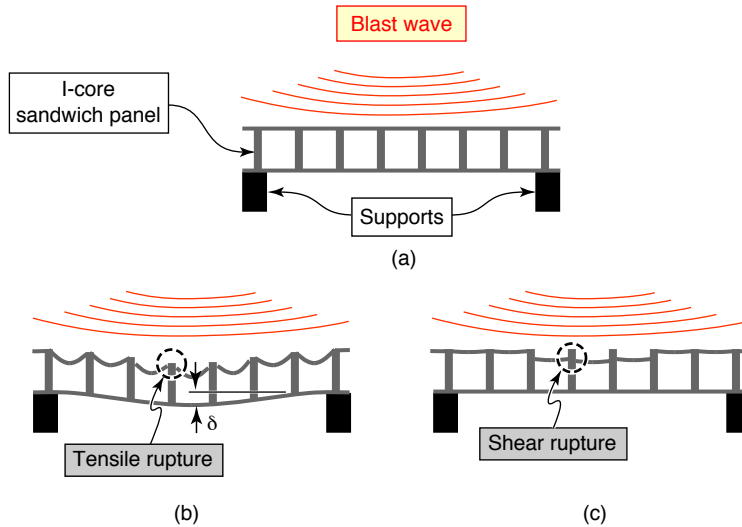
Figure 1. (a) Impingement of a blast wave onto an I-core sandwich panel with an I-core that resists crushing. (b) For moderately high impulse intensity, the face sheets undergo significant plastic bending and stretching, followed by tensile rupture. (c) At high impulse intensity, face failure occurs by *shear rupture* at the junctions with the core members shortly after impingement of the pressure wave and prior to significant deformation elsewhere, with minimal global deformation.

Experiments on impulsively loaded clamped plates reveal similar characteristics (Figure 3) [Menkes and Opat 1973; Nurick and Shave 1996]. (i) At low impulse I the plates plastically bend and stretch without rupture and the plate deflection increases monotonically with I. (ii) At intermediate I, plate stretching is followed by tensile rupture at the supports. In this domain, the degree of plastic stretching preceding rupture *diminishes* with increasing I. (iii) At high I, failure occurs by shear rupture at the supports *prior to macroscopic deformation*. For response (iii), once rupture is complete, the plate retains most of its kinetic energy and thus represents a significant remnant threat.

To probe response (iii), a high-speed impact test that duplicates the deformation of the plates at the supports has been devised and analyzed. It involves projecting hard cylinders into plates of the targeted materials and monitoring changes in projectile velocity as penetration occurs (similar to that of [Borvik et al. 2002a; 2002b]). It is demonstrated that, given an appropriate combination of sheet thickness and projectile velocity, penetration occurs through intense shear deformation and rupture along an annular ring concentric with the projectile. This mechanism is deemed the same as that experienced by the faces of impulsively-loaded panels locally, where they attach to the supports and core members. Namely, the failure criterion determined from the projectile tests is considered suitable for analysis of impulse-induced face shear-off. To devise a viable failure criterion, a numerical analysis is used to model the penetration and seek a consistent correlation with the experiments.

The article is organized as follows. The experimental protocols and test results are summarized in Sections 2 and 3. Details of the finite element model including the mesh design, the material constitutive
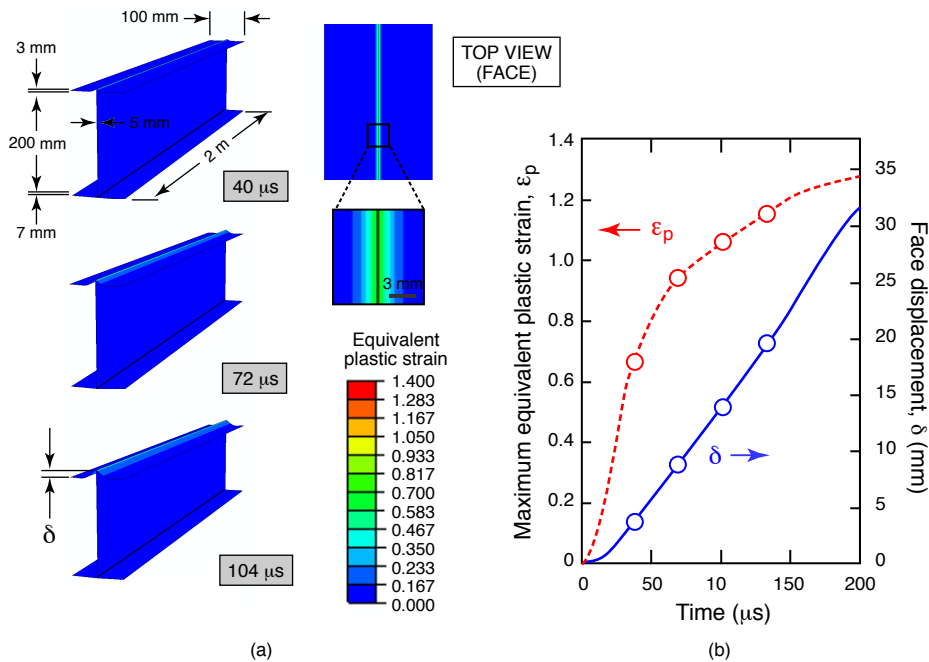
Figure 2. Evolution of peak plastic strain and displacement of the wet face in an I-core panel subject to a water blast (free-field peak pressure $= 200$ MPa, decay time $= 100\,\mu$s, impulse intensity $= 20$ kPa·s). Periodic boundary conditions are applied to the sides of the unit cell shown in the series on the left. The edges of the bottom face are rigidly clamped. Times are those after initial impingement of the pressure wave on the wet face. Material properties are those of 304 stainless steel. (Courtesy A. Spuskanyuk, UCSB).

laws, and the rupture criterion, are presented in Section 4. Section 5 contains the numerical results as well as comparisons with experimental measurements.

2. Testing procedures

Projectile impact tests were performed using a single-stage gas gun (Figure 4). The gun consists of a pressurized chamber, a 5 m long, 0.30 caliber (7.62 mm diameter) barrel, and an intervening diaphragm that ruptures at a specified chamber pressure. Flat-ended cylindrical projectiles (25.4 mm in length and 7.54 mm in diameter) were fabricated from A2 tool steel and heat-treated to a hardness of 58 Rockwell C. Either nitrogen or helium was used for pressurization. Projectile velocities were controlled through selection of the diaphragm material (copper or stainless steel) as well as its thickness. Exit velocities were measured by three pairs of infrared sensors attached to the muzzle break at the end of the barrel. The velocities employed in the present study span the range 200–400 m/s. This velocity range corresponds to an initial plate momentum of approximately 2.5–5 kPa-s for the 1.5 mm plate and 5–10 kPa-s for the 3 mm plate; these are comparable to impulse intensities of present interest.

Two steels were tested: 304 stainless steel (SS) and superaustenitic AL6XN. The specimen dimensions were 70 mm × 70 mm, with thickness of either 1.52 mm or 3.05 mm. Specimens were rigidly clamped
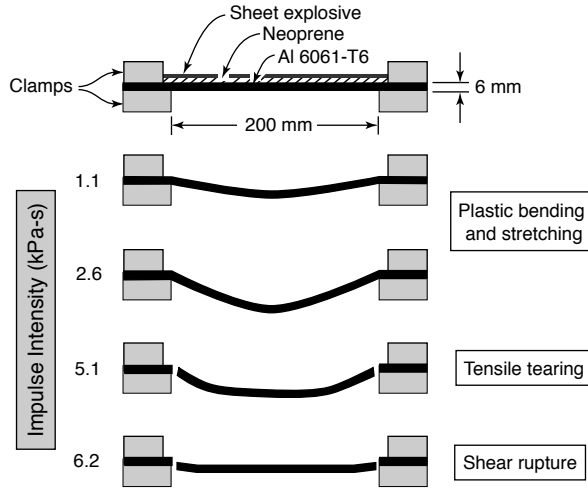
Figure 3. Transitions in deformation and failure modes in an Al alloy plate subject to increasing impulse intensity. Specimens are 25 mm wide. Impulsive loads are applied by detonation of a sheet explosive adhesively bonded to the top surface. (Adapted from [Menkes and Opat 1973].)

around their periphery leaving a central area, 50 mm × 50 mm, exposed. The fixture was attached to a steel catch chamber filled with sand to arrest the projectile and the resulting plug with little additional damage. The sides of the fixture were fabricated from clear polycarbonate to facilitate viewing by a high-speed digital camera (Imacon 200, DRS Technologies). The images were used to determine both
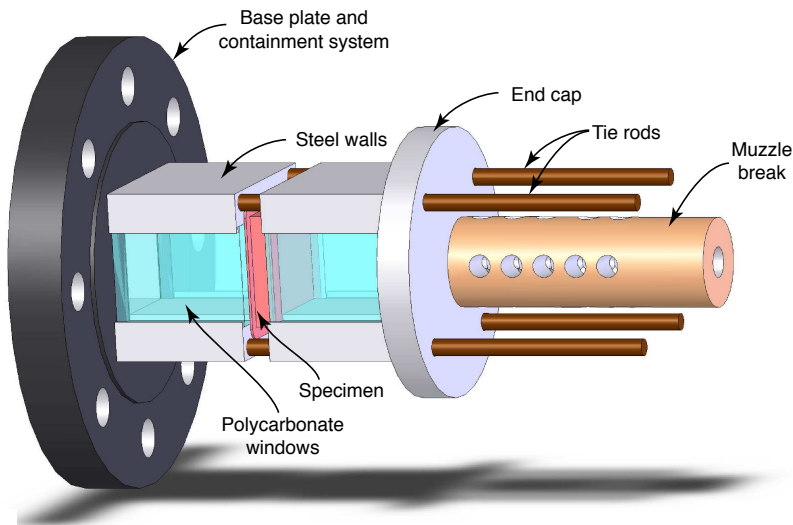

Figure 4. Schematic of test fixture.

incident and exit velocities of the projectile via calibrated image analysis software (DRS Technologies). The resolution of these measurements was ~ 2 m/s.

Following testing, normal deflections of the impacted surface were measured using a depth gauge at various radial distances from the hole edge. In some cases, the specimens were subsequently sectioned along a diametral plane through the hole in order to document the deflection profiles. Changes in projectile diameter at the impacting surface were also measured using a micrometer.

To establish a baseline of mechanical properties, quasistatic uniaxial tensile tests were performed on dog-bone specimens of both materials at a nominal strain rate of 10^{-3} s^{-1}. The true (logarithmic) tensile failure strain was obtained from areal measurements on optical micrographs of the fracture surfaces in combination with the measured initial cross-sectional area.

3. Experimental results

Typical photographic sequences showing projectile impact and penetration are presented in Figure 5. In all cases, fracture occurred along a well-defined annular ring concentric with the cylindrical surface of the projectile, thereby producing a cylindrical plug (Figure 6) and a corresponding hole in the plate

304 SS: h=1.52 mm,
v_0 = 296 m/s, Δt_i = 18 µs

AL6XN: h=3.05 mm,
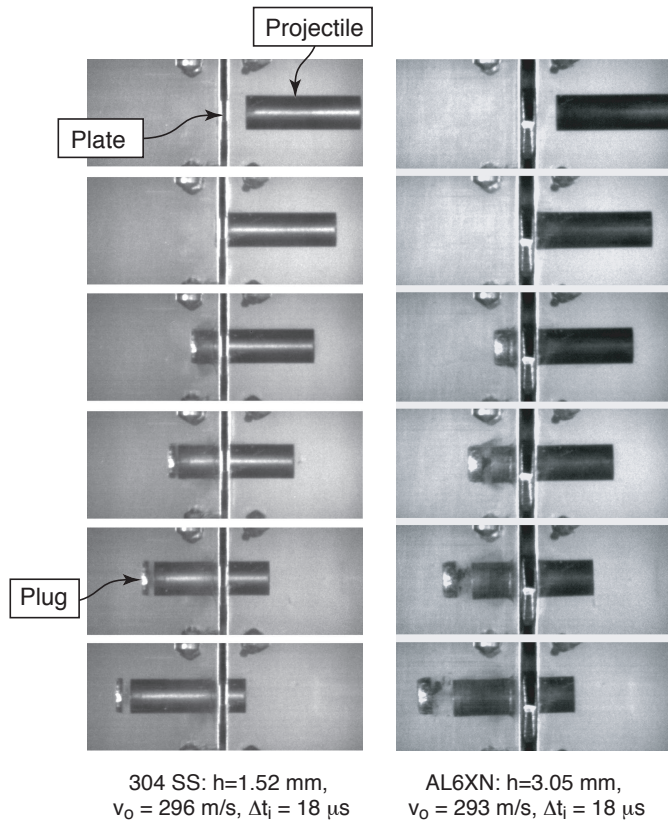v_0 = 293 m/s, Δt_i = 18 µs

Figure 5. High speed photographs showing plug formation and projectile penetration from two representative tests (Δt_i is time between frames).
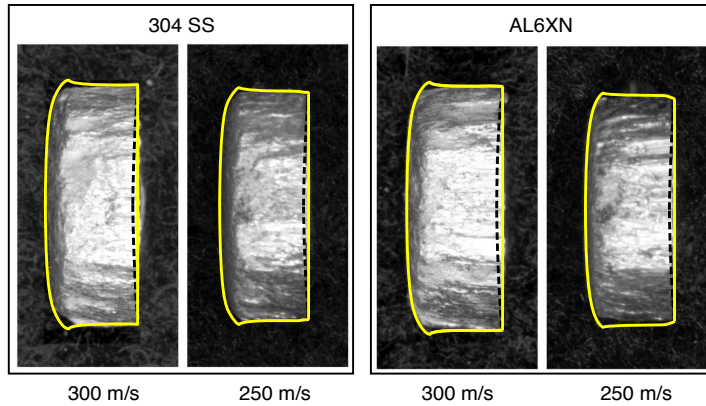
Figure 6. Photographs of typical plugs formed by projectile penetration tests. Solid overlaid lines are predicted projected shapes from the numerical simulations. The dashed lines represent the plug shape through the diametral plane (not visible in the actual plugs).

(Figure 7). The projectiles typically exhibited some "mushrooming" on the impacting face (Figure 8). The diametral strains ranged from 1 to 8%, increasing with both projectile velocity and plate thickness.

Changes in projectile velocity, Δv, with incident velocity, v_o, are plotted on Figure 9. Also shown are two boundaries that define the accessible domain. An upper bound is set by the ballistic limit, whereupon $\Delta v \leq v_o$. A lower bound is obtained by equating the momentum of the incident projectile with that of both the exiting projectile and the resulting plug for a material with zero failure strain [Teng and Wierzbicki
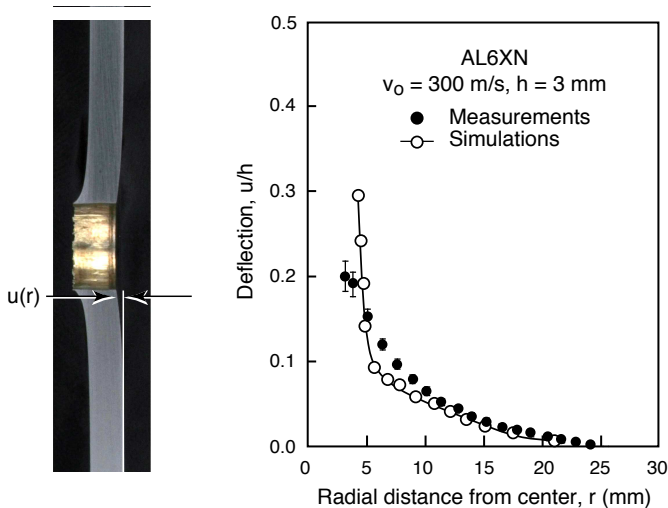

Figure 7. (a) Cross-sections through plates after testing. (b) Experimental measurements and numerical predictions of plate deflection. The latter correspond to a time $t v_o / h = 14$ after projectile impact.
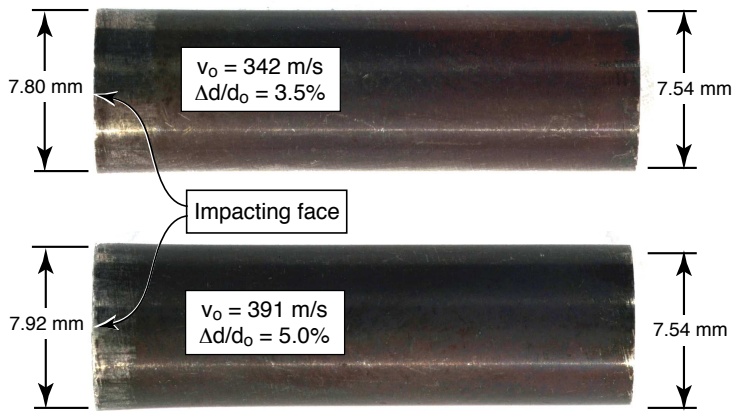
Figure 8. Projectiles after penetration through 3 mm thick plates.

2005]. Upon assuming that the plug diameter and density are the same as those for the projectile, the resulting requirement on velocity is: $\Delta v \geq v_o(1 + L_{pr}/h)^{-1}$ where L_{pr} is the projectile length. All experimental data fall in the allowable domain.

At low v_o, Δv initially decreases with v_o, attains a minimum, and thereafter rises approximately linearly with v_o. The latter appears to be essentially parallel to the boundary defined by momentum
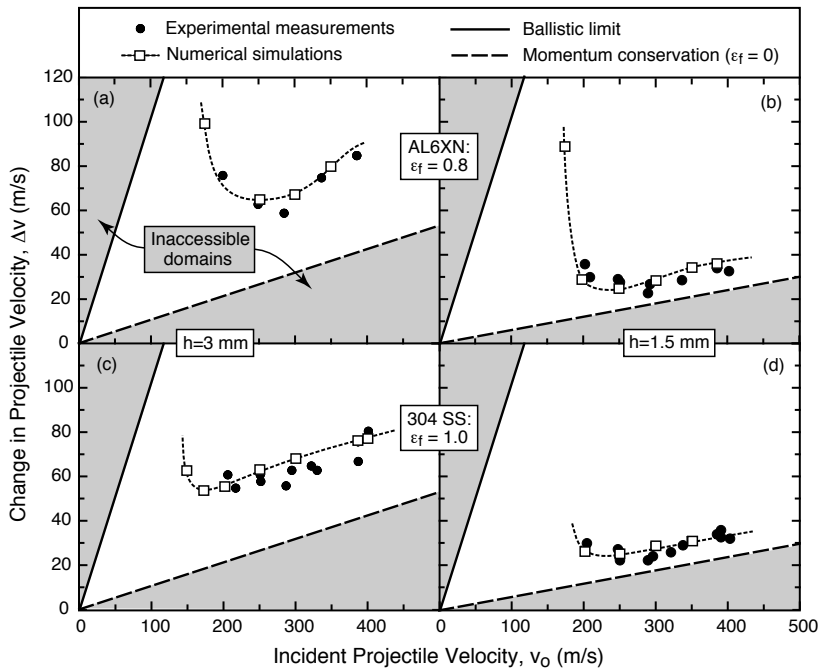

Figure 9. Changes in projectile velocity with incident velocity for (a, b) AL6XN and (c, d) 304 SS, for two plate thicknesses (1.5 and 3 mm).
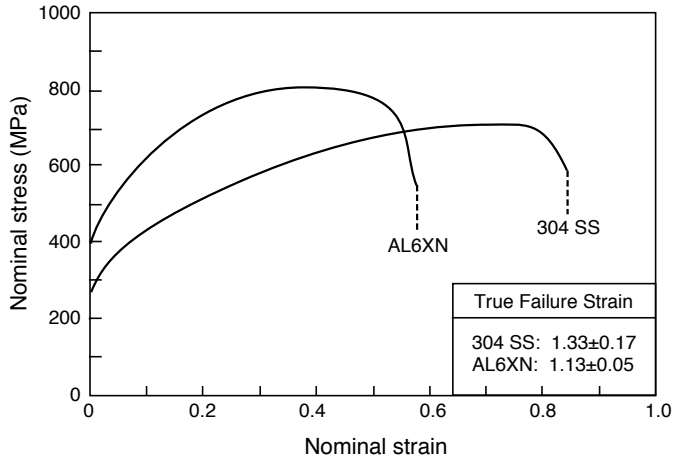
Figure 10. Quasistatic tensile stress-strain curves of both materials. Failure strains were calculated from area measurements at the fracture plane.

conservation. The inference is that the velocity change due to plug formation (above that needed to accelerate the plug) is insensitive to v_o.

The quasistatic tensile properties are summarized in Figure 10. The stress-strain curves are used subsequently in calibrating the constitutive law for the finite element model, incorporating strain-rate and temperature sensitivity data from other studies [Liu and Guo 2000; Nemat-Nasser et al. 2001]. The tensile failure strains for both materials are high, falling in the range 1.1–1.3.

4. Finite element model

Dynamic finite element calculations of the shear-out tests were performed using the finite element code ABAQUS Explicit 6.5-1. The strain required for shear rupture was inferred from comparisons of measured and simulated projectile velocities.

4.1. *Mesh design.* Given the cylindrical geometry of the projectile and the highly localized deformation pattern in the vicinity of the shear-out zone, an axisymmetric model was employed. The mesh near the shear-out zone was highly refined. In most cases, the mesh elements were $14\,\mu m$ and $71\,\mu m$ in the radial and through-thickness directions, respectively. These dimensions were selected to be comparable to typical shear band widths in the steels of interest: notably 10–$100\,\mu m$ [Borvik et al. 1999]. Elsewhere, the meshes were significantly coarsened. The total element count was 20,000 and 6,000 for the 3 mm and 1.5 mm plates, respectively. Both the plate and the projectile were meshed using four-node bilinear elements with reduced integration and hourglass section control (CAX4R in [ABAQUS 2005]). A typical mesh in the plate near the shear zone beyond the end of the projectile is illustrated in Figure 11. Boundary conditions were applied such that the outside edge of the plate was restricted from translation and rotation. Initial conditions consisted of a uniform initial velocity applied to the projectile.

When a *fixed mesh* was employed, the finite element calculations failed to converge after about half of the projectile had passed through the plate, a consequence of severe material deformation in the ruptured elements. It will become apparent, though, that these calculations adequately capture the penetration
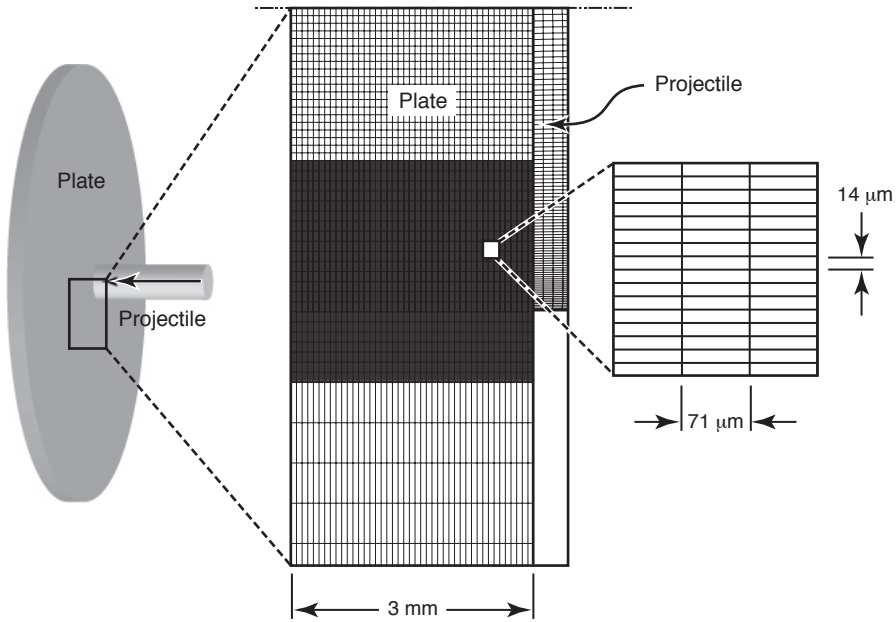
Figure 11. Finite element model used to simulate shear-out tests.

process and the associated changes in projectile velocity. They are, however, unable to predict the final plate shape because of the retained elastic deformation at the instant of penetration and the subsequent spring back. In an attempt to probe the pertinent features over longer times, additional calculations were performed using an *adaptive meshing* scheme. By moving the mesh independently of the material while keeping the mesh topology and number of elements fixed, the adaptive scheme yields a high-quality mesh even when severe deformation occurs [ABAQUS 2005]. Comparisons with the fixed mesh simulations confirmed that the two schemes yield essentially identical results at short times (wherein the fixed mesh calculations converge).

4.2. *Constitutive laws.* The dynamic plastic response of the plates was modeled using the Johnson–Cook constitutive law [Johnson and Cook 1985]. The flow stress is given by:

$$\sigma_y = [A + B(\varepsilon_e^{pl})^n]\left[1 + C\ln\left(\frac{\dot{\varepsilon}_e^{pl}}{\dot{\varepsilon}_0}\right)\right](1 - \theta^m), \tag{1}$$

where $\dot{\varepsilon}_0$ is a reference strain rate, ε_e^{pl} is the equivalent plastic strain, $\dot{\varepsilon}_e^{pl}$ is the equivalent plastic strain rate, A, B, C, n, and m are experimentally derived material constants, and θ is a normalized temperature defined by

$$\theta = \frac{T - T_{tr}}{T_M - T_{tr}}, \tag{2}$$

with T being absolute temperature, T_M the melting temperature, and T_{tr} a transition temperature (taken as ambient). Material heating due to plastic deformation is assumed to occur adiabatically with 90% of

	E(GPa)	ν	ρ(kg/m^3)	A(MPa)	B(MPa)	C	n	m	$\dot{\varepsilon}_0$(s^{-1})	T_{tr}(K)	T_M(K)	C_p(J/kg-K)
304 SS	193	0.3	7800	310	1000	0.034	0.65	1.05	0.001	293	1800	450
AL6XN	161	0.35	7850	400	1500	0.045	0.4	1.2	0.001	293	1800	452

Table 1. Summary of parameter values for Johnson–Cook constitutive law.

the plastic work converted into heat, such that the temperature increase ΔT at any material point is

$$\Delta T = \frac{0.9}{\rho c_p} \int \sigma_{ij} d\varepsilon_{ij}^p. \tag{3}$$

The pertinent material parameters were obtained from the quasistatic tensile tests (for strain hardening parameters A, B and n) coupled with complementary data for rate and temperature sensitivity (to obtain C and m) [Liu and Guo 2000; Nemat-Nasser et al. 2001]. All parameter values are listed in Table 1. Because of the small strains experienced by the projectiles, their material behavior was treated as elastic-perfectly plastic with a yield strength (2.0 GPa) selected to be consistent with the measured hardness (58 Rockwell C) and independent of strain rate.

4.3. *A rupture criterion.* The rupture criterion is based on a critical value of the equivalent plastic strain, ε_f, assumed to be independent of strain rate and stress triaxiality as will be justified in a subsequent discussion. Formally, the criterion can be expressed in terms of a damage parameter, ω, defined as

$$\omega = \int \frac{d\varepsilon_e^{pl}}{\varepsilon_f}.$$

Failure is predicted when ω reaches unity. Once this criterion is satisfied, the properties of the failed element are modified such that only compressive stresses can be supported. This effectively creates a mode II (shear) crack that cannot transmit either shear or normal tensile stresses. (In preliminary studies, element deletion was eliminated as a potential alternative because it removes excessive amounts of material leading to unrealistic relaxation of the constraints in the shear-out zone.) The utility of using ε_f as a consistent failure criterion for each material is assessed below by comparing the predicted changes in projectile velocity with the experimental measurements.

Because of the absence of a material length scale in the failure criterion, the predictions of the numerical simulations are inherently mesh-size dependent [Needleman and Tvergaard 1994; Gullerud et al. 2000]. The mesh size, coupled with the failure strain, dictate the amount of localized deformation that occurs along the fracture plane (closely analogous to the critical displacement in cohesive zone formulations). The intrinsic crack tip toughness is thus expected to be proportional to $w\varepsilon_f$ (w being the element width). In addition to its role in determining toughness, the mesh size governs the resolution of the predicted strain distribution adjacent to the crack plane and, in turn, the accuracy of the global response metrics. Consequently, with the current approach, the selected mesh must be sufficiently fine to ensure adequate strain resolution yet be representative of the intrinsic width of the fracture process zone.

Most of the present simulations were based on a mesh with $14 \times 71 \, \mu$m elements, which (as demonstrated below) are sufficiently refined to accurately resolve the plasticity and are broadly consistent with the scale of the fracture process zone (10–100 μm). Using this mesh, ε_f was inferred from changes in projectile velocity, Δv, with incident velocity, v_o, for both plate thicknesses and alloy types. To assess mesh-size effects, additional calculations were performed using finer ($10 \times 50 \, \mu$m) and coarser ($35 \times 145 \, \mu$m) elements. The assessment was made on the basis of the predicted Δv and the strain distribution.

5. Numerical results

5.1. *Projectile penetration and velocity change.* The stages of plate failure predicted by the finite element simulations are illustrated in Figure 12. An annular shear crack concentric with the projectile axis initiates shortly after impact. For the case shown, the nondimensional initiation time is $tv_o/h \approx 0.15$ (h/v_o representing the time needed for the projectile to travel a distance equal to the plate thickness at its initial velocity). Thereafter, the crack propagates at a speed 1–4 times that of the projectile. Full crack penetration is obtained before the projectile has traveled one plate thickness ($tv_o/h < 1$). During this process, plastic deformation is localized within a narrow annular band adjacent to the crack surface. Some plastic deformation also occurs within the projectile shortly after impact. The larger projectile diameter
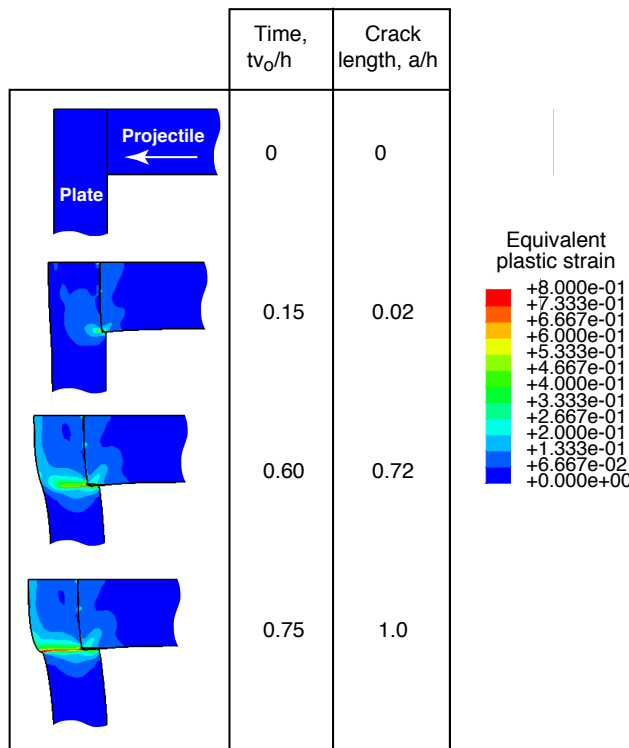

Figure 12. Evolution of plastic strain and crack growth for a 3 mm thick AL6XN plate impacted by a projectile with initial velocity $v_o = 300$ m/s.

effectively increases the failure zone diameter and serves to increase the area over which intense plastic deformation occurs. Plate bending and stretching are negligible until the crack approaches the back surface. As $a/h \rightarrow 1$, the remaining ligament ruptures in a tensile mode.

The kinetic energy lost by the projectile is dissipated mainly by plastic deformation, both in the projectile and the shear zone of the plate. The evolution of kinetic energy, U_k, and plastic dissipation, U_p, is shown in Figure 13. Over the time period $0 \leq tv_o/h \leq 1$, U_k diminishes rapidly as U_p increases. For this specific case, about 60% of the dissipation occurs within the plate and the plug, the balance occurring within the projectile. During this period, plastic deformation in the shear zone causes a maximum temperature increase of about 300 K. The end of this stage is marked by complete crack penetration. Thereafter, the projectile kinetic energy approaches a steady-state value with small oscillations caused by reflecting stress waves. The expected period of oscillation, $t_{osc}v_o/h = v_o L_{pr}\sqrt{\rho}/h\sqrt{E} = 0.5$ (ρ being mass density and E the Young's modulus), is in excellent agreement with the numerical results. The plug kinetic energy also reaches a steady state shortly after crack penetration.

Although the kinetic energy of the plate (without the plug) represents a small fraction of the total, it exhibits oscillations with a long period (typically $t_{osc}v_o/h = 5$), a consequence of remnant plate vibration.
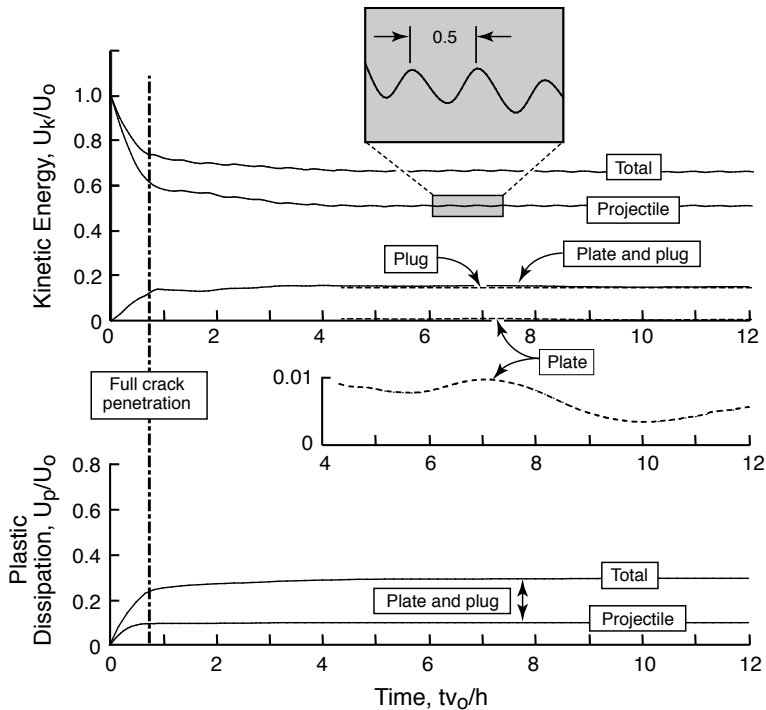

Figure 13. Evolution of kinetic energy and plastic dissipation during a shear out test (AL6XN, $h = 3$ mm, $v_o = 300$ m/s, $\varepsilon_f = 0.8$). Insets in the top graph illustrate the oscillatory nature of projectile and plate kinetic energies as well as the pertinent time scales. U_o is the initial projectile kinetic energy.

The vibration persists for times well beyond those of the present simulations. The consequences are evident in the remnant plate shape, described below (Section 5.3).

The predicted changes in Δv with v_o are plotted on Figure 9. For 304 SS, it is apparent that all results are well reproduced for a fixed failure strain, $\varepsilon_f \approx 1.0$. Similar consistency is apparent for AL6XN, albeit for a slightly lower critical strain, $\varepsilon_f \approx 0.8$. Attaining such consistency over a wide range of parameter space provides justification for application of the critical strain approach to shear rupture in these materials. The inferred values represent about 70% of the respective tensile failure strains under quasistatic loading (Figure 10).

An assessment of the selected element size ($14 \times 71\,\mu$m) was made by examining the plastic strain distributions in the vicinity of the crack. Results for a 3 mm thick AL6XN plate impacted by a projectile with initial velocity $v_o = 300$ m/s, at a crack length $a/h \approx 0.6$, are plotted on Figure 14(a). The distributions correspond to three trajectories perpendicular to the crack plane: one passing through the crack tip (A) and the other two (B and C) at distances of 0.07 mm (one element) and 0.14 mm (two elements) ahead of the tip (see inset). With this mesh, the plastic zone is spread over many elements ($\gg 10$) on either side of the crack plane. The conclusion is that the mesh is sufficiently refined to accurately resolve the plasticity.

The evolution of the stress triaxiality around the crack tip for this mesh is plotted on Figure 14(b). Although the crack propagates nominally in mode II, finite triaxiality is obtained at its tip. Moreover, the triaxiality increases slightly with crack growth, from about $-1/3$ for short cracks to about $1/3$ for long cracks. The latter is consistent with a purely tensile rupture in the final stages of penetration arising from plate bending and stretching. Nevertheless, these levels of triaxiality are deemed to be small (in relation to those obtained in mode I for example) and justify neglect of the triaxiality dependence of the failure strain in the present model.

5.2. *Mesh sensitivity.* Mesh sensitivity effects were probed by comparing the preceding results with those obtained using coarser and finer meshes. The resolution of the resulting strain distributions (Figure 15) for the two finer meshes ($10 \times 50\,\mu$m and $14 \times 71\,\mu$m) is deemed to be adequate. In contrast, the coarsest mesh yields unacceptable results.

The coupled effects of mesh size and failure strain on the projectile velocity change are illustrated in Figure 16(a). Significant mesh sensitivity is evident (although the results for the coarsest mesh are likely inaccurate because of the poor strain resolution). Since the global dissipation (characterized by the change in kinetic energy of the projectile and the plug) is expected to scale with the intrinsic crack tip toughness [Tvergaard and Hutchinson 1992; Suo et al. 1993], and the tip toughness is proportional to $w\varepsilon_f$, it follows that the global dissipation should also be proportional to $w\varepsilon_f$. When the numerical results are plotted accordingly (Figure 16(b)), it becomes evident that the dissipation does indeed scale with $w\varepsilon_f$ for the two finer meshes, with the proportionality constant being only weakly dependent on ε_f. In the limit where $w \to 0$, the tip toughness vanishes and no global dissipation is obtained. Consequently, efforts to further refine the mesh to increase the strain resolution would have the adverse effect of yielding anomalously low dissipation. This scaling seemingly fails for the coarsest mesh, again likely a manifestation of the poor strain resolution.

5.3. *Remnant deformation.* A secondary assessment of the numerical model was made by comparing the predicted shapes of the plugs with those observed experimentally. Predicted shapes are overlaid on
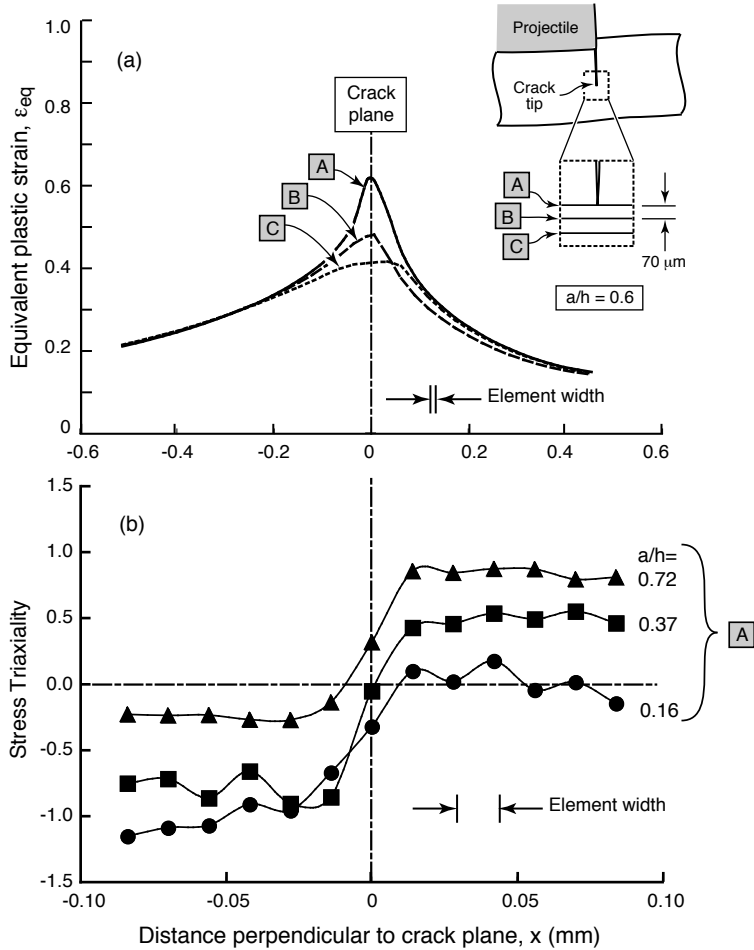
Figure 14. (a) Distribution of equivalent plastic strain ahead of a crack tip during shear-out. For the mesh size employed here ($14\,\mu\mathrm{m} \times 71\,\mu\mathrm{m}$), the zone of intense plasticity is spread over many elements, thereby precluding the anomalous localization that occurs with a coarser mesh (compare with Figure 15i). (b) Corresponding stress triaxiality at various crack lengths, a/h. The triaxiality along the failure plane ($x = 0$) varies from about $-1/3$ to $1/3$.

the corresponding photographs in Figure 6. The only detectable discrepancy is in the flaring of the plug near the face opposite that being impacted; this feature is predicted but not evident experimentally. It is attributable to slight rotation of the elements during the final stages of fracture (due to plate bending and stretching), coupled with restrictions on crack path imposed by element shape.

Additionally, an attempt was made to predict the shape of the plate after penetration. One set of results is plotted on Figure 7. Although the agreement with the experimental measurements appears
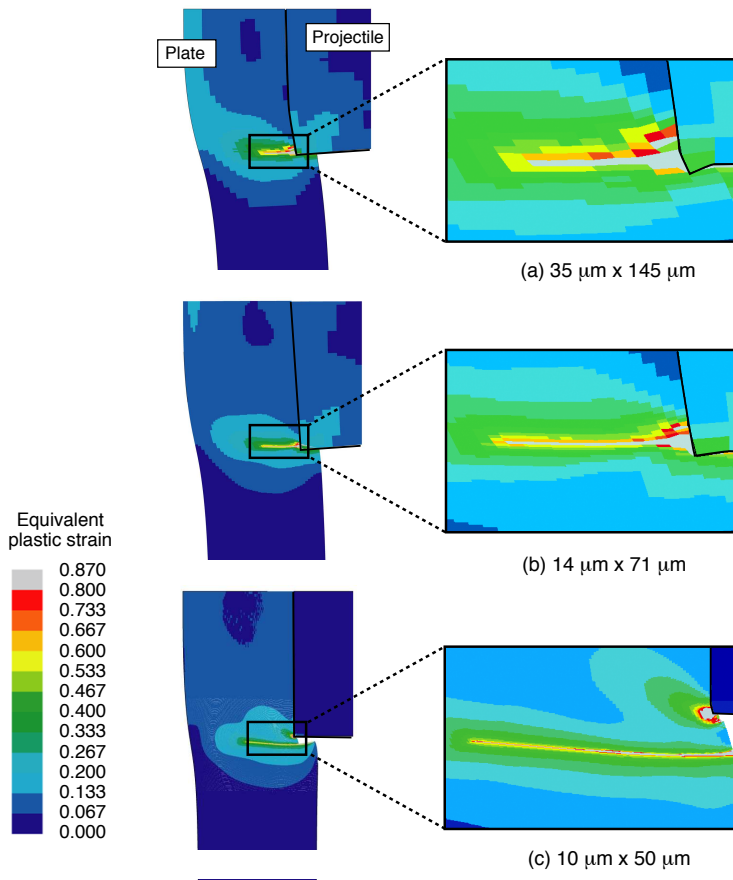
Figure 15. Effects of mesh size on plastic strain distributions around the crack tip ($\varepsilon_f = 0.8$).

reasonable, the accuracy of the predictions is compromised by plate vibrations that persist well after complete penetration. The vibration is evident in the oscillations in both the kinetic energy (Figure 13) and the plate deflection (Figure 17) with time. Accurate predictions would require significant extensions in the simulation times. Because each "long" simulation (with adaptive meshing) required several days to complete, the additional computational effort needed to properly simulate the plate defection is deemed impractical. The conclusion is that plate deflection is a poor metric for assessment of the model.

6. Concluding remarks

A methodology for ascertaining the dynamic shear rupture strain of metal plates has been devised and demonstrated. Using a critical plastic strain criterion for rupture, the predictions of the numerical model agree well with the experimental measurements on two stainless steel alloys over a range of projectile velocities and plate thicknesses. The failure strains inferred in this manner represent about 70% of the corresponding quasistatic tensile failure strain. However, the inferred strains are strictly valid only when used with the specified mesh.
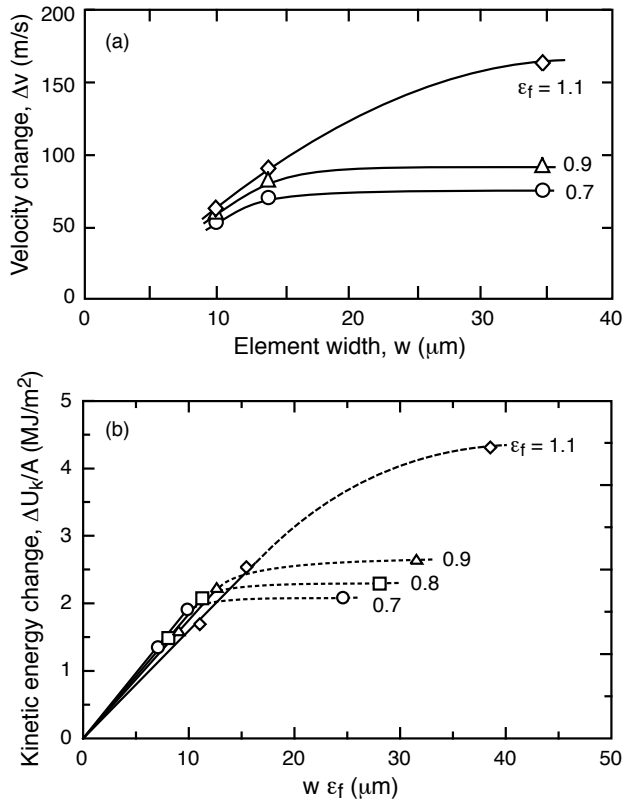
Figure 16. Effects of mesh size and failure strain on (a) predicted projectile velocity and (b) change in kinetic energy of the plate and the plug, normalized by the nominal crack area, A. (Same case as that in Figure 13).
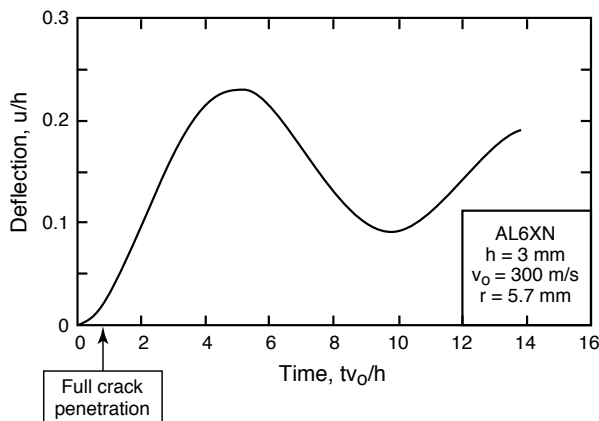

Figure 17. Temporal variation in plate deflection at a point on the impacted surface 5.7 mm from the hole center (same case as that in Figure 13). The plate remains in motion at the end of the simulation.

Generally, selection of the mesh size for this class of problems is dictated by three factors. (i) For realism, the mesh size should be broadly consistent with the known dimensions of the fracture process zone (typically 10–100 μm in ductile steels). (ii) The mesh in the vicinity of the crack plane should be sufficiently refined to ensure acceptable resolution in the predicted plastic strains. Otherwise, the accuracy of the plastic dissipation and other metrics associated with the global response will be inaccurate. (iii) Excessive refinement should be avoided, since it leads to unrealistically low dissipation while also greatly increasing computational time. Moreover, it may require the use of unrealistically high failure strains in order to match predictions with experimental measurements. The expectation is that a reasonably broad range of mesh sizes should satisfy these criteria and yield acceptable predictive capability, provided the failure strain is selected consistently with the mesh size.

References

[ABAQUS 2005] Providence, R.I: Abaqus Inc., *ABAQUS/Explicit User's Manual, Version 6.5-1*, Providence, R.I: Abaqus Inc., 2005.

[Borvik et al. 1999] T. Borvik, M. Langseth, O. S. Hopperstad, and K. A. Malo, "Ballistic penetration of steel plates", *Int. J. Impact Eng.* **22** (1999), 855–86.

[Borvik et al. 2002a] T. Borvik, O. S. Hopperstad, T. Berstad, and M. Langseth, "Perforation of 12 mm thick steel plates by 20 mm diameter projectiles with flat, hemispherical and conical noses: part II: numerical simulations", *Int. J. Impact Eng.* **27**:1 (2002), 37–64.

[Borvik et al. 2002b] T. Borvik, M. Langseth, O. S. Hopperstad, and K. A. Malo, "Perforation of 12 mm thick steel plates by 20 mm diameter projectiles with flat, hemispherical and conical noses: part I: experimental study", *Int. J. Impact Eng.* **27**:1 (2002), 19–35.

[Gullerud et al. 2000] A. S. Gullerud, X. Gao, B. Dodds Jr., and R. Haj-Ali, "Simulation of ductile crack growth using computational cells: numerical aspects", *Eng. Fract. Mech.* **66** (2000), 65–92.

[Johnson and Cook 1985] G. R. Johnson and W. H. Cook, "Fracture characteristics of three metals subjected to various strains, strain rates, temperatures and pressures", *Eng. Fract. Mech.* **21** (1985), 31–48.

[Liang et al. 2007] Y. Liang, A. V. Spuskanyuk, S. E. Flores, D. R. Hayhurst, J. W. Hutchinson, R. M. McMeeking, and A. G. Evans, "Response of metallic sandwich panels to water blasts", *J. Appl. Mech.* **74**:1 (2007), 81–99.

[Liu and Guo 2000] C. R. Liu and Y. B. Guo, "Finite element analysis of sequential cuts and tool-chip friction on residual stresses in a machined layer", *Int. J. Mech. Sci.* **42** (2000), 1069–1086.

[Menkes and Opat 1973] S. B. Menkes and H. J. Opat, "Tearing and shear failure in explosively loaded clamped beams", *Exp. Mech.* **13** (1973), 480–486.

[Needleman and Tvergaard 1994] A. Needleman and V. Tvergaard, "Mesh effects in the analysis of dynamic ductile crack growth", *Eng. Fract. Mech.* **47**:1 (1994), 75–91.

[Nemat-Nasser et al. 2001] S. Nemat-Nasser, W. G. Guo, and D. P. Kihl, "Thermomechanical response of AL6-XN stainless steel over a wide range of strain rates", *J. Mech. Phys. Solids* **49** (2001), 1823–1846.

[Nurick and Shave 1996] G. N. Nurick and G. C. Shave, "The deformation and tearing of thin square plates subjected to impulsive loads- an experimental study", *Int. J. Mech. Sci.* **18**:1 (1996), 99–116.

[Suo et al. 1993] Z. Suo, C. F. Shih, and A. G. Varias, "A theory for cleavage cracking in the presence of plastic flow", *Acta Metall. Mater.* **41**:5 (1993), 1551–1557.

[Teng and Wierzbicki 2005] X. Teng and T. Wierzbicki, "Dynamic shear plugging of beams and plates with an advancing crack", *Int. J. Impact Eng.* **31** (2005), 667–698.

[Tvergaard and Hutchinson 1992] V. Tvergaard and J. W. Hutchinson, "The relation between crack growth resistance and fracture process parameters in elastic-plastic solids", *J. Mech. Phys. Solids* **40**:6 (1992), 1377–1397.

KEN NAHSHON: ken.nahshon@navy.mil
Division of Engineering and Applied Sciences, Harvard University, Cambridge, MA 02138, United States

MICHAEL G. PONTIN: mpontin@engineering.ucsb.edu
Materials Department, University of California, Santa Barbara, CA 93106-5050, United States

ANTHONY G. EVANS: agevans@engineering.ucsb.edu
Materials Department, University of California, Santa Barbara, CA 93106-5050, United States

JOHN W. HUTCHINSON: jutchins@fas.harvard.edu
Division of Engineering and Applied Sciences, Harvard University, Cambridge, MA 02138, United States

FRANK W. ZOK: zok@engineering.ucsb.edu
Materials Department, University of California, Santa Barbara, CA 93106, United States